Tomographic shadowgraphy for spray diagnostics

J. Klinner, C. Willert
Institute of Propulsion Technology, German Aerospace Center (DLR), 51170 Köln
GERMANY

Abstract

This contribution introduces 3-D shadowgraphy which is capable of resolving the placement of the liquid phase within a certain spray volume both spatially and temporally. The method is based on a multiple view camera setup and inline illumination provided by current pulsed LEDs. The quality of spray reconstruction was investigated using experimental data from multiple view shadowgraphs of hollow cone and flat fan water sprays. After calibration and determination of a 3-D mapping function for each view a line-of-sight (LOS) intensity reconstruction was implemented. After sequential combination of back-projected images at each voxel plane of the volume the 3-D droplet and ligament positions can be readily obtained. Further improvement of intensity reconstruction may be achieved by a iterative tomographic reconstruction, namely multiplicative algebraic reconstruction technique (SMART). These improvements are documented by comparing slices of the averaged 3-D shadowgraph intensity of the hollow cone spray orthogonal to the flow. The investigations were further substantiated with simulations using synthetic data to estimate reconstruction quality at increasing droplet densities.

Introduction

The dispersion of liquid kerosine films or jets by swirling airblast atomizers in gas turbine combustors is driven by a highly three-dimensional flow. Aircraft atomizers are usually of pre-filming type, where kerosine is spread out in a thin continuous sheet, or of injector type, where fuel is introduced as jets in cross flow. As the liquid sheet or jet is usually exposed in between two coaxially counter-rotating (pronounced shear layer) or co-rotating (wide spray angle) flows, 3-D-trajectories of liquid structures, ligaments and droplets are dominant. Diagnostic methods capable of mapping the 3-D placement of atomized fuel within the combustion volume spatially and temporally, even under non-reactive conditions, is therefore highly desirable.

Using inline holography Miller and Sallam [12] have investigated the liquid breakup of aerated water injectors with $d_0 = 0.5 - 1.0mm$ in crossflow at a momentum flux ratio q of about 90. They concluded that in high particle density regions strong reference beam obscuration and speckle noise problems occur which lead to low resolution. Further the limited angular aperture of digital inline holograms leads to a depth of focus which is in the order of millimeters for droplets of $10 - 20$ μm size [11]. Reconstructed intensities of droplet shapes are therefore several orders of magnitude elongated in axial length. Cao et al [4] have developed a improved holographic setup for dense sprays by combining the inline reference beam with a side scattered object wave. This reduces the scattered intensity range and therefore allows the resolution of higher order side lobes of the diffraction pattern and therefore increases axial resolution. They were able to measure the 3-D particle distribution in isotropic turbulence in a volume of $8 \times 6 \times 10$ mm^3 at number densities of 4.2 p/mm^3. A technique referred to as tomographic digital holographic PIV was introduced by Soria and Atkinson [18] and involved crossing several inline holographic setups. However the advantage of such dual- or multi-beam interferometric setups require a higher instrumentation effort. In order to obtain information on droplet velocity multi-pulsed lasers are required.

Within this contribution the potential of tomographic intensity reconstruction, based on spray shadow imaging from multiple views, is investigated. Tomographic intensity reconstruction techniques such as multiplicative algebraic reconstruction techniques (MART) [5] [7], simultaneous MART (SMART) [13] and multiplicative line-of-sight (MLOS) [1], minimum line-of-sight (MINLOS) [10] and synthetic aperture refocusing (SAR) [2] have been intensively developed within the recent years. Most of these techniques are primarily optimized for the particle field reconstruction for tomographic particle image velocimetry (tomo-PIV). In the field of spray investigation additional issues are of interest such as the ability to localize and characterize larger non-spherical structures of primary atomization at all stages of liquid film or jet disintegration which incorporates dilational or sinuous oscillations, perforated-sheet disintegration and ligament formation at the leading edges [9].

The herein proposed spray reconstruction technique termed *tomographic shadowgraphy* relies on shadow images of sprays obtained by four-view observation arrangement using inline illumination with incoherent pulsed LED light for each view. After thorough calibration, spray ligaments and droplets are reconstructed by means of

*Corresponding author: joachim.klinner@dlr.de

an in-house line-of-sight (LOS) reconstruction technique. By sequential combination of back-projected images at each voxel plane of the volume the 3-D droplet and ligament positions can be readily obtained. In comparison to the frequently used iterative algebraic reconstruction techniques this approach allows a fast image reconstruction with low memory demand which makes it particularly attractive for aerosol particle tracking at high data rates. In addition to experimental aspects and results obtained with tomographic shadowgraphy this contribution investigates the quality of the 3-D LOS intensity reconstructions of the hollow cone in comparison to an iterative SMART reconstruction. The comparison is based on averaged tomographic shadowgraphy intensity distributions.

Due to the limited number of projections the reconstruction of a collection of droplets within a volume leads to ambiguities that depend on droplet density, viewing geometry and camera resolution. This is caused by intersections of the line-of-sights of different droplets with each other and results in the formation of so-called *ghost particles* [5],[1]. In order to estimate the ghost particle rate for a non-iterative LOS reconstruction, the experimental viewing geometry of each camera was simulated by a pinhole camera model which uses physical imaging parameters including camera yaw, tilt, magnification and resolution. Images of synthetic particle volumes are rendered according to this model and later reconstructed by LOS techniques. As a measure of reconstruction quality the 3-D cross-correlation coefficient between reconstruction and known particle distribution was evaluated [5].

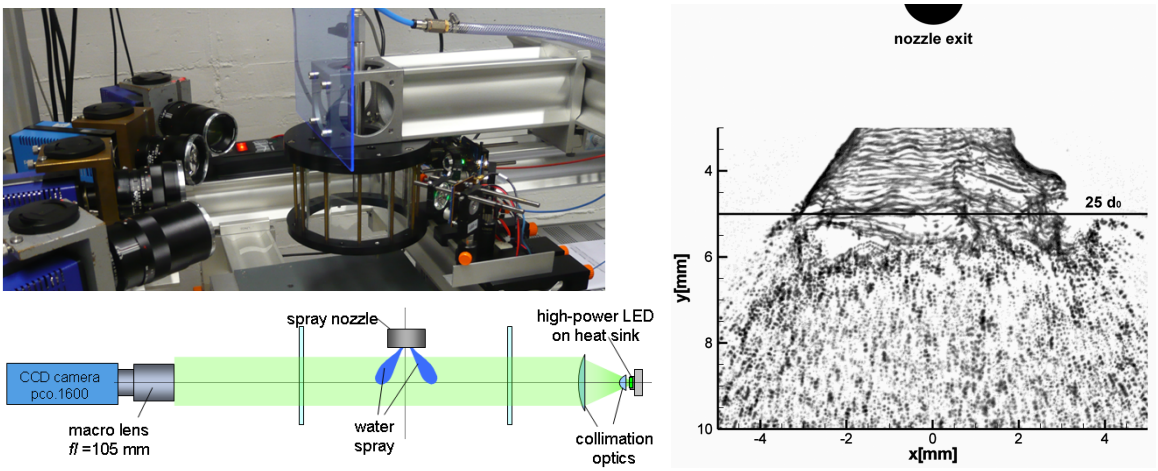

Figure 1. Left: Experimental setup for tomographic shadowgraphy; right: section of back-projected double exposed shadowgraph (View 2), axis orthogonal slices of the reconstructed volume of the hollow cone spray are extracted at $y = 25\,d_0$

Materials and Methods

Experimental setup

The experimental set-up for tomographic shadowgraphy shown in **Fig.** 1 involved four synchronized double-frame (PIV) cameras angled 30° with respect to each other and observed a water spray which was injected in a 12-sided polygon-shaped chamber at atmospheric pressure. The hollow cone spray was dispersed by a pressure-driven simplex swirl nozzle with $d_0 = 0.2$ mm and 63° spray angle while the flat fan spray was created with a flat-fan nozzle with $d_0 = 0.23$ mm and spray angle of 65°. The water injection pressure was fixed at 6 bar in order to have spray not fully developed within the imaged region immediately downstream of nozzle exit. This allowed the observation of all stages of liquid disintegration from film breakup into ligaments and further into droplets.

Inline illumination is provided for each camera by a current pulsed high power green LED (Luminus, SST-90, green) whose light is collimated with aspheric condenser lens [20]. Peak currents between $I_{\mathrm{f,max}} = 10 - 25$ A at $\tau_{\mathrm{p}} = 1$ μs were found sufficient to provide bright-field intensity levels at half camera dynamic range at lens apertures $f_{\#} = 16 - 22$. The pulse separation was $\Delta t = 6.4$ μs. Focus depth of each tilted camera was optimized by a Scheimpflug-adapter. Using macroscopic imaging lenses with small apertures, a common volume of approx. $18 \times 18 \times 10$ mm^3 could be imaged with minimal blurring due to depth of field variations. The respective exposure parameters are summarized in table 1. Camera resolution of each view was 1600×1200 pixel at a mean magnification of 60 pixel/mm or approx. $M = 0.5$. The pixel size is 7.4 μm which is below the diffraction limited droplet image size d_{A} listed in table 1 and given by [14]:

$$d_{\mathrm{A}} = 2.44 f_{\#}(M+1)\lambda \tag{1}$$

If droplets are approximately of size d_{A}/M diffraction limited imaging rather than geometric imaging becomes

Table 1. Shadowgraphy setup parameters

view	$\approx \varphi$	$f_\#$	$f\ [mm]$	$\approx M$	d_A [μm]	$I_\mathrm{f,max}$ [A]
1	45°	22	100	0.45	39	25
2	15°	16	85	0.43	28	9.9
3	-15°	16	85	0.44	28	10
4	-45°	22	100	0.43	38	26

dominant. Thus, in theory, particle images can not further downsized optically and therefore the reconstructed droplet sizes will likely be larger than the real size.

Volumetric camera calibration and intensity reconstruction

Lithographic photomasks with checkerboard patterns on soda-lime glass were used as calibration target which was backlit with a display LED for homogenous illumination. Opaque regions consist of a 100 nm thick layer of chromium oxide. The lateral dimensional tolerance of the corner positions is $\pm$300 nm. The traversal of calibration pattern along z-axis by a motorized translation stage finally allowed the sequential recording of 3-D points in space at a positioning accuracy better than ± 2 μm. Each calibration set consisted of ten z positions each with 23×17 corners at a $1\,mm$ spacing.

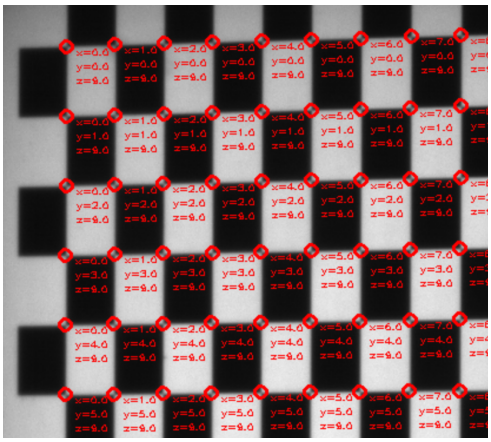

Figure 2. Section of the assigned grid of View 2. of a single plane, world coordinates in [mm]

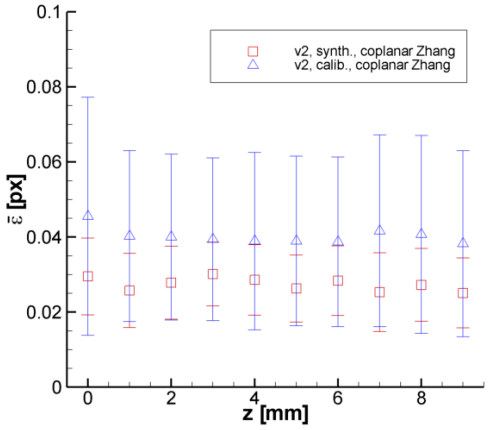

Figure 3. Back-projection error for View 2 with coplanar Zhang-calibration, synth: synthetic calibration of ideal pinhole camera

Point correspondence in checkerboard images were found in two steps. After applying an adaptive thresholding, second order partial derivatives of image are formed, followed by a local smoothing. The derivatives are then combined by means of Harris corner detection[6]. Corners coincide with local intensity peaks in the result image. Sub-pixel accuracy in the vicinity of these peaks is achieved by iterative searching the radial saddle point of intensity as described in [3]. This allows sub-pixel detection accuracies better than 0.1 pixel [8]. An exemplary result is shown in **Fig.** 2

A volumetric intensity reconstruction from multiple views requires an accurate assignment of world and image coordinates. This is done by mapping functions which are either based on physical camera parameters and perspective equation or consist of higher order local polynomials to directly compensate distortions [17]. Frequently used photogrammetric camera models in computer vision (e.g. Tsai's model [19]) are based on a pinhole camera model and differ mostly in terms of parameterizations and in the modeling of lens distortions [15]. Volume mapping parameter for camera calibration are derived from planar homographies as described in [8]. For implementation of the corner detection, grid assignment and camera calibration according to Zhang [21] the C/C++ OpenCV library

2.0 and PivMap3.0 software (PIVTEC GmbH, Germany) were used. A comparison of the accuracy of different photogrammetric and polynomial mapping approaches in accordance with the experimental setup is described in [8]. The deep volume calibration accuracy was determined from the averaged residuals of the back-projection error for each calibration plane **Fig.** 3. The error at each calibration-point in image space is given by the magnitude of the difference vector between projected point coordinates and measured coordinates:

$$\epsilon_i = \sqrt{(x_{Ii} - x_{Pi})^2 + (y_{Ii} - y_{Pi})^2} \tag{2}$$

It turned out that a pinhole camera model with compensation of radial and tangential lens distortions as described in [3] can provide rather low averaged back-projection errors for each calibration plane and each view of $\overline{\epsilon_i} < 0.05$ pixel.

The shadowgraphy intensities are inverted and adjusted by a sliding minimum subtraction. The reconstructed volume size is $18 \times 17.25 \times 9$ mm^3 which corresponds to $1081 \times 1036 \times 541$ voxel at 60 voxel/mm. The observed intensities of each voxel are found according to its line-of-sight intersection with each image plane. These positions are calculated from planar mappings obtained from calibration as described in [8]. Sub-pixel intensities are calculated by bilinear interpolation of the 4-connected pixel. The observed intensities from each view are combined either by geometric average, by multiplication (MLOS) or by applying a minimum operator (MINLOS). The MLOS reconstruction of a double exposure of $1081 \times 1036 \times 541$ voxel from four views took in the order of 5 min on a single-core 2.53 GHz processor. **Fig.** 4, right, shows a MLOS reconstruction of a single realization of the fan spray for a $4 \times 4 \times 4$ mm^3 partial volume at a resolution of $256 \times 256 \times 256$ voxel. The corresponding location of this region is indicated in the shadowgraph image left. Single droplets and parts of ligaments can be identified showing the liquid sheet disintegration in three dimensions. The arrow marks comparable shapes on the edge of the liquid film.

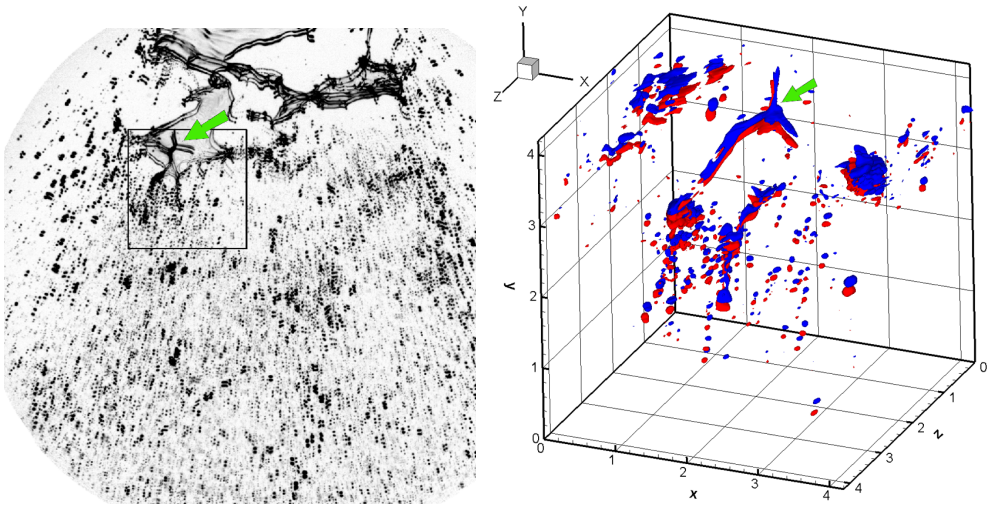

Figure 4. Left: Shadowgraph image pair of a flat fan spray; one of four simultaneous views; right: iso-intensity plot of the spray within region indicated by the rectangle in the shadowgraph. Blue represents the reconstruction obtained for the first recording while red was acquired 6.3 μs later in time

The iterative SMART reconstruction further refines for instance MLOS initialized voxel intensities [1] by repeated projection of voxel intensities onto each image plane followed by a voxel intensity correction according to recorded image intensities. Projecting, comparing and updating the voxel intensity for all views is done in one iteration loop and repeated until the projected intensities converge. Convergence of experimental data occurred after 20 iterations. The 20 SMART iterations for one double-exposure took in the order of 18 min on a 12-core Intel Xeon System at 2.66 GHz.

Estimation of the limiting droplet number density for a LOS reconstruction

The expected reconstruction quality versus droplet number density was estimated by a numerical simulation. For this purpose a synthetic volume of $500 \times 500 \times 250$ voxel was filled with uniformly distributed intensity blobs of Gaussian shape at 3 voxel diameter and particle numbers of 1000, 2000, 4000, 8000, 16000 corresponding to number densities of 3.5, 7, 14, 28, 56 p/mm^3 with 60 voxel/mm scaling. The viewing geometry of each camera

according to experimental conditions was simulated by a photogrammetric pinhole camera model **Fig.** 5:

$$w \cdot \begin{bmatrix} x_I \\ y_I \\ 1 \end{bmatrix} = \begin{bmatrix} sf & 0 & c_x \\ 0 & sf & c_y \\ 0 & 0 & 1 \end{bmatrix} \cdot \begin{bmatrix} \mathbf{R}|\mathbf{t} \end{bmatrix} \cdot \begin{bmatrix} x \\ y \\ z \\ 1 \end{bmatrix} \tag{3}$$

The left matrix, which is frequently refereed as camera matrix **A**, contains the parameter s which describes the sensor resolution in pixel/mm, f is the effective focal length in [mm], c_x, c_y describe the intersection between optical axis and senor in pixel. The center was placed at half synthetic image width and height. The translation vector **t** [mm] points from world coordinates origin toward the center of projection (location of lens principal point). **R** and **t** form the 3×4 matrix **W**. The rotation matrix **R** is calculated from Euler-angles sensor yaw (φ around Y axis) and pitch (ψ around new X axis):

$$\mathbf{R} = \begin{bmatrix} 1 & 0 & 0 \\ 0 & cos\,\psi & sin\,\psi \\ 0 & -sin\,\psi & cos\,\psi \end{bmatrix} \cdot \begin{bmatrix} cos\,\varphi & 0 & -sin\,\varphi \\ 0 & 1 & 0 \\ sin\,\varphi & 0 & cos\,\varphi \end{bmatrix} \tag{4}$$

Synthetic image generation requires the projection of synthetic volume intensities onto the virtual image plane which is done by the inversion of **Eq.** (3) for each plane z_i in the volume. Calculating the homography $\mathbf{H} = \mathbf{A} \cdot \mathbf{W}$ with the constraint $z = const$ results in a regular invertible 3×3 matrix that describes the back-projection of image coordinates to world coordinates for plane $z = z_i$:

$$w \cdot \begin{bmatrix} x_z \\ y_z \\ 1 \end{bmatrix} = \mathbf{H}_z^{-1} \cdot \begin{bmatrix} x_I \\ y_I \\ 1 \end{bmatrix} \tag{5}$$

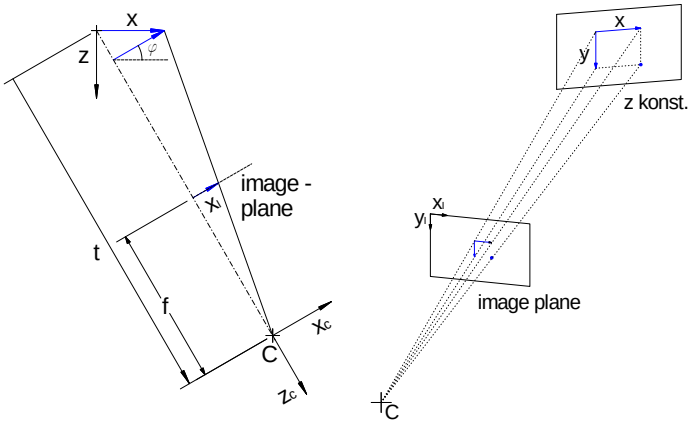

Figure 5. Pinhole camera model: Converting from object to camera coordinate system

Projected image intensities are obtained by bilinear interpolation of nearest neighbor voxel intensities. Image intensities are calculated by summing the projections from each plane z_i. Particle image densities of simulated view 2 are shown in **Fig.** 7, left. Reconstruction quality was estimated by the degree of correlation between synthetic volume (ground truth) and reconstruction, which is given by the cross-correlation coefficient c_{II} [14] also referred to as quality factor [5]. Using a interrogation volume of 64^3 voxel at a step size of 32^3 in total $14 \times 14 \times 6$ positions of the reconstructed and ground truth particle field were correlated. The averaged degree of correlation versus particle density is plotted in **Fig.** 7, right.

Results and Discussion

Fig. 6 shows a cross section of the hollow cone spray at $y = 25\,d_0$ as processed with four different reconstruction methods using identical image preprocessing. The volume sections represent the average of 266 reconstructed 3-D shadowgraphs. The connected circular shape indicates regions where strong light deflection occur. This coincides with the rim of the liquid conical sheet and with regions where ligaments and droplets appear frequently. Further downstream (i.e. $y > 25\,d_0$, not shown here) the degree of atomization increases and the averaged intensities are spread over a larger circular area.

The LOS reconstructions show more blurred intensities compared to the SMART results. The intensity is partially spread along lines-of-sight. The multiplicative combination of back-projected intensities shows the best suppression of these artifacts and results in the highest local gradients close to the ring when compared to the minimum and geometric average image combination. The averaged iterative SMART reconstruction shows a more focused circular shape with higher intensity gradients close to the ring and and therefore may deliver a more accurate result. However this involves roughly a 50 times longer computational effort.

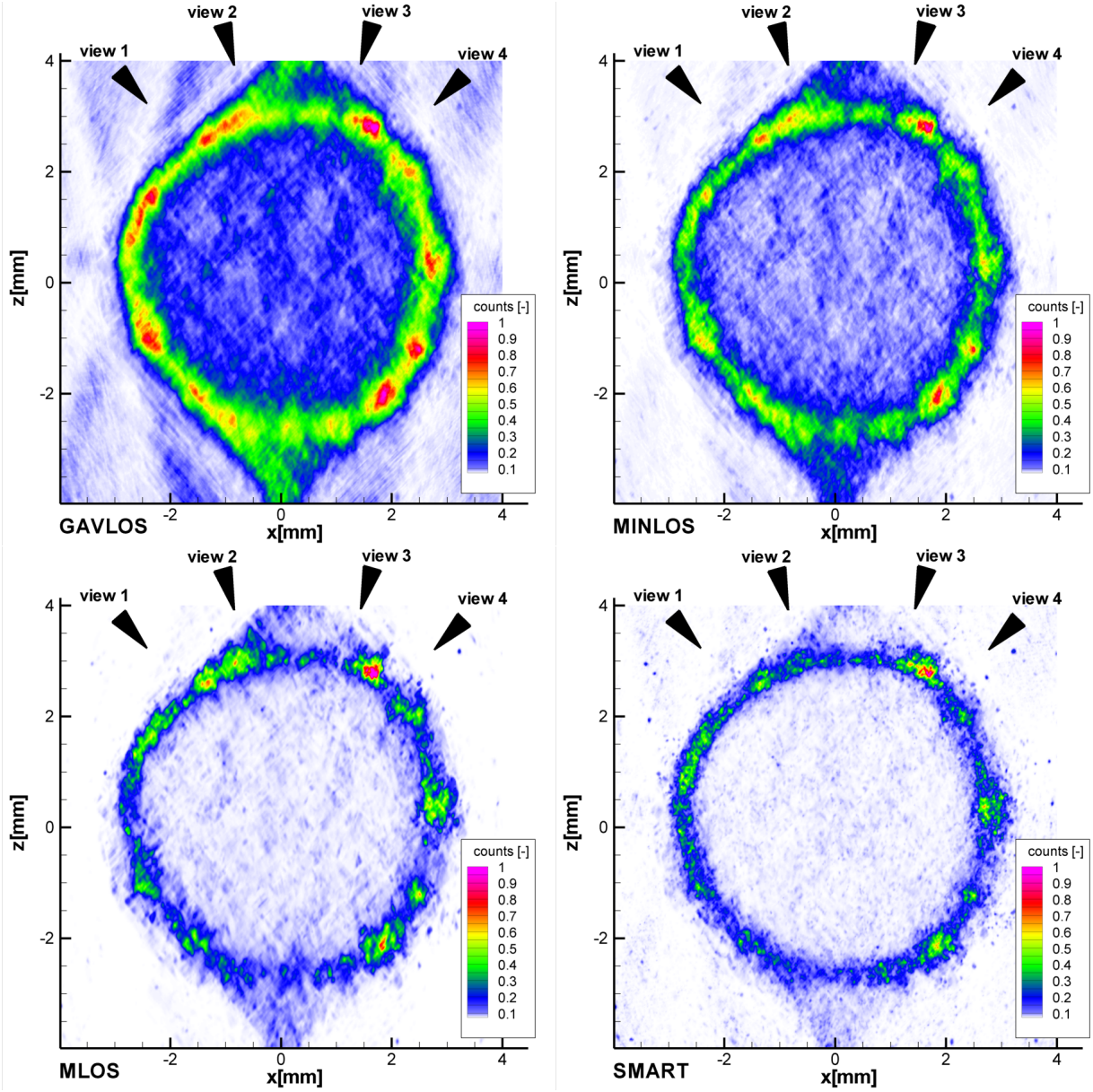

Figure 6. Extracted slices of 266 averaged volume reconstructions of the hollow cone spray at $y = 25\,d_0$; in direction of reading 1: geometric average (GAVLOS), 2: minimum (MINLOS) and 3: multiplication (MLOS) of back-projected intensities,4: SMART reconstruction after 20 iterations

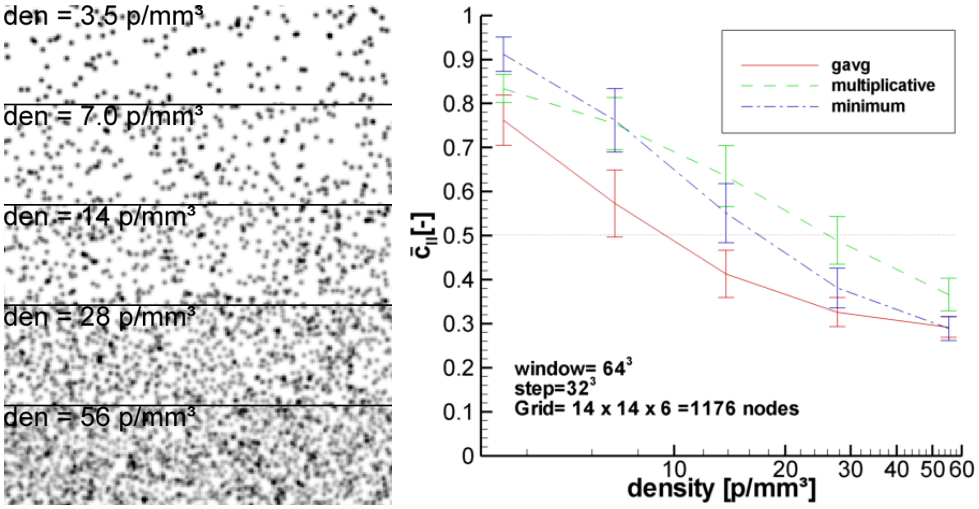

Figure 7. Left: sections of synthetic view 2 (negated intensities) of simulated particle volumes at $500 \times 500 \times 250$ voxel; right: 3D-cross-correlation coefficient at different combinations of line-of-sight intensities

According to numerical simulation results in **Fig.** 7 the decreasing of reconstruction quality of LOS with increasing droplet number density is reproduced. Highest degree of correlation between ground truth and reconstruction above densities of 7 $\mathrm{p/mm^3}$ is obtained by a multiplicative intensity combination.

Conclusion and outlook

A proposed technique called *tomographic shadowgraphy* demonstrated that instantaneous spray structures can be recovered by tomographic reconstruction of multi-view shadowgraphs of the liquid phase. Compared to holographic methods the instrumentation effort is much reduced. The use of pulsed LED illumination in place of lasers further reduces complexity and cost. Using high speed cameras the method can be extended to provide time-resolved, three-dimensional data of the spray development.

The rather efficient reconstruction speed of the line-of-sight reconstruction allows the technique to be used for statistics calculation over many realizations to arrive at volume resolved mean droplet distributions. The reconstructed volume data is well suited to extract additional information such as droplet velocities and trajectory with 3-D particle tracking velocimetry (PTV). Moreover the development of the spray can be investigated in detail to estimate the local breakup-length. Using SMART reconstruction at increasing droplet number densities provides a better suppression of ghost droplet intensities at the cost of a considerably higher computational effort. According to the results of a numerical simulation the recovery of droplets at particle densities up to 20 $\mathrm{p/mm^3}$ is possible for the applied camera configuration and a MLOS reconstruction (assuming a quality factor of greater than 0.5). Further numerical investigations have to be carried out to estimate ghost particle rates for the respective camera configuration.

Acknowledgments

The SMART implementation and the corresponding Matlab calibration routine [16] was kindly provided by the Department Experimental Methods of the Institute of Aerodynamics and Flow Technology of the German Aerospace center (DLR).

Nomenclature

c_{II}	cross-correlation coefficient
d_0	nozzle orifice diameter
d_{A}	Airy disk diameter
f	focal length
$f_{\#}$	f-number
$I_{\mathrm{f,max}}$	maximum continuous forward current
M	magnification
s	sensor resolution [pixel/mm]

Δt	delay between two illumination pulses (for PIV)
q	jet/freestream momentum flux ratio
w	arbitrary scale factor in projective geometry
ϵ	back-projection error
λ	wavelength of light
τ_p	pulse duration
φ	camera yaw angle (around world y axis)
ψ	camera pitch angle (around new x axis after φ-rotation)

Subscripts

P	projected coordiantes
I	image coordinates

References

[1] C. Atkinson and J. Soria. An efficient simultaneous reconstruction technique for tomographic particle image velocimetry. *Experiments in Fluids*, 47:553–568, 2009.

[2] J. Belden, T. T. Truscott, M. C. Axiak, and A. H. Techet. Three-dimensional synthetic aperture particle image velocimetry. *Measurement Science and Technology*, 21(12):125403, 2010.

[3] G. Bradski and A. Kaehler. *Learning OpenCV*. O' Reilly Media, Inc., Sebastopol, 1th edition, 2008.

[4] L. Cao, G. Pan, J. Jong, and H. Woodward S.and Meng. Hybrid digital holographic imaging system for three-dimensional dense particle field measurement. *Appl. Opt.*, 47(25):4501–4508, Sep 2008.

[5] G. Elsinga, F. Scarano, B. Wieneke, and B. van Oudheusden. Tomographic particle image velocimetry. *Experiments in Fluids*, 41:933–947, 2006.

[6] C. Harris and M. Stephens. A combined corner and edge detector. In *4th Alvey Vision Conference*, pages 147–151, 1988.

[7] G. T. Herman and A. Lent. Iterative reconstruction algorithms. *Computers in Biology and Medicine*, 6(4):273 – 294, 1976.

[8] J. Klinner and C. Willert. The implementation of tomographic shadowgraphy for spray diagnostics. In *9th International Symposium on Particle Image Velocimetry – PIV 11*, July 2011.

[9] A. H. Lefebvre. *Atomization and Sprays*. CRC Press Taylor & Francis Group, 1989.

[10] H.G. Maas, P. Westfeld, T. Putze, N. Boetkjaer, J. Kitzhofer, and C. Brücker. Photogrammetric techniques in multi-camera tomographic PIV. In *8th International Symposium on Particle Image Velocimetry - (PIV09), Melbourne, Australia*, 2009.

[11] H. Meng, G. Pan, Y. Pu, and S. H. Woodward. Holographic particle image velocimetry: from film to digital recording. *Measurement Science and Technology*, 15(4):673, 2004.

[12] B. Miller, K. A. Sallam, K.-C. Lin, and C. Carter. Digital holographic spray analyzer. In *ASME Conference Proceedings of 14th International Conference on Nuclear Engineering (FEDSM2006)*, volume 2, pages 1023–1028, 2006.

[13] D. Mishra, K. Muralidhar, and P. Munshi. A robust MART algorithm for tomographic applications. *Numerical Heat Transfer, Part B: Fundamentals*, 35(4):485–506, 1999.

[14] M. Raffel, C. Willert, S. Wereley, and J. Kompenhans. *Particle Image Velocimetry, A Practical Guide*. Springer Berlin-Heidelberg, 2007.

[15] J. Salvi, X. Armangué, and J. Batlle. A comparative review of camera calibrating methods with accuracy evaluation. *Pattern Recognition*, 35(7):1617 – 1635, 2002.

[16] D. Schanz, S. Gesemann, A. Schröder, B. Wieneke, and D. Michaelis. Tomographic reconstruction with non-uniform optical transfer functions (otf). In *15th Int Symp on Applications of Laser Techniques to Fluid Mechanics*, July 2010.

[17] S. M. Soloff, R. J. Adrian, and Z-C. Liu. Distortion compensation for generalized stereoscopic particle image velocimetry. *Measurement Science and Technology*, 8(12):1441, 1997.

[18] J. Soria and C. Atkinson. Towards 3c-3d digital holographic fluid velocity vector field measurement - tomographic digital holographic PIV (Tomo-HPIV). *Measurement Science and Technology*, 19(7):074002, 2008.

[19] R.Y. Tsai. A versatile camera calibration technique for high-accuracy 3d machine vision metrology using off-the-shelf tv cameras and lenses. *IEEE J. Robot. Autom.*, RA-3:323–344, 1987.

[20] C. Willert, B. Stasicki, J. Klinner, and S. Moessner. Pulsed operation of high-power light emitting diodes for imaging flow velocimetry. *Measurement Science and Technology*, 21(7):1–12, 2010.

[21] Z. Zhang. A flexible new technique for camera calibration. Technical report, Microsoft Research, 1999.